

Chapter 5

Depolarisation upon multiple scattering

In the earlier chapters, we have shown how polarisation can be used to discriminate between the ballistic and diffuse light. We employed this principle in two situations, namely imaging and coherent backscattering. In this chapter, we shall examine in detail, the process of depolarisation, the influence of scatterer anisotropy and the implications of these to imaging.

5.1 Introduction

Wave transport in scattering media has been extensively investigated experimentally and theoretically[1, 2, 3]. The diffusion approximation, which assumes that light becomes diffusive inside a random medium, has been employed in most analytical approaches and has explained to various extents, a variety of observed phenomena, such as the temporal point spread function of a random medium, the enhancement of backscattered intensity and depolarisation of polarised light upon multiple scattering[4, 5, 6, 7, 8]. However, as recent experiments have pointed out[9, 10, 11, 12, 13], caution has to be exercised in applying the diffusion approximation to scattering samples which are thin, or are illuminated by collimated light, or have significant absorption. The diffusion theory presumes that, upon entering a multiply scattering medium, the propagation of light is rendered diffusive within

a distance of a transport mean free path, $l^*[1, 2]$. However, it has been experimentally established that the first few scattering events are not capable of completely destroying the direction memory of light, and non-diffusive transport occurs upto depths of several transport mean free paths. The study regarding the exact depth at which the ballistic transport converts to diffusive transport, i.e. the ballistic to diffuse transition, has become a separate field of activity in itself[14, 15, 16, 17]. The fact that such non-diffusive transport exists has been put to use in biomedical optics in imaging of objects inside turbid media.

Several schemes exist that utilise the forward scattered snake light for imaging. As explained in the chapter 3, we had devised a scheme to extract two-dimensional images from random media using polarisation modulation[18]. On the numerical front, we had also studied the randomisation of the photon direction using Monte Carlo simulations, and put forth an empirical definition of 'diffuse' photons[19]. The dependence of randomisation of direction of propagation was studied as a function of scattering anisotropy. In this chapter, we present the results of our experimental and numerical studies of randomisation of polarisation inside the turbid medium. We illustrate in the course of this chapter, that randomisation of the direction of propagation and randomisation of polarisation occur at greatly different length-scales. This complements the earlier work, and helps in understanding the depth of imaging using polarisation preservation of the quasiballistic photons. We have used the technique of polarisation modulation to study the depolarisation inside the random medium, for scatterers with various anisotropies. A Monte-Carlo simulation of a three-dimensional random walk of photons was carried out, in which the polarisation of the photon and the direction of propagation were kept track of after each scattering event. We have simulated random photon paths inside media of various thicknesses, and examined the depolarisation over a considerable range of anisotropies. We compare the utility of the polarisation gating technique for scattering phantoms of different anisotropies, and reassert that one can image deeper inside a medium composed of isotropic scatterers. We also show that this technique can improve the image contrast and

the resolution of images obtained by fourier gating or by temporal gating, especially in case of samples with isotropic scatterers.

5.2 Experimental details

The experimental setup used to study the polarisation preservation is shown in figure 5.1. and is the same as described in earlier chapters. The setup incorporates the principle of fourier spatial filtering, and has the additional feature of polarisation gating.

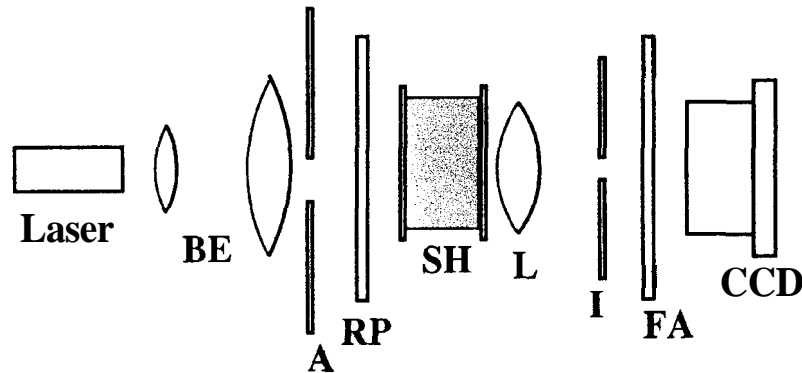


Figure 5.1: *Experimental setup for studying the depolarisation of light in a multiply scattering medium. BE : Beam Expander, A : Aperture, RP : Rotating Polariser, SH : Sample Holder, L : Lens, I : Iris, FA : Fixed Analyser.*

A He-Ne laser beam ($\lambda=612$ nm, unpolarised) was expanded using a beam expander to a diameter of about 6 mm. An aperture of diameter 2.8 mm was used to extract a working beam with flat intensity profile. The beam was passed through a polariser that could be rotated about the Z axis, collinear with the beam, using a stepper motor, thus enabling the rotation of the plane of polarisation of the beam through any desired angle. The power of the beam after passing through the polariser was about 0.5 mW. The beam was normally incident on a sample holder that is cylindrical in shape and coaxial to the beam. The sample holder was so designed that its length could be varied continuously from 0 mm to 40 mm, and thus, with a given l^* , samples of varying optical thickness could be obtained. The scattering samples used were colloidal suspensions

of polystyrene microparticles in deionised water. Suspensions of different particle sizes ($a = 0.12, 0.192, 0.21$ and 0.23 microns) were used to make scattering samples with differing anisotropies ($g = 0.117, 0.302, 0.375,$ and 0.45 respectively). For each particle size, a single colloidal suspension of known scatterer concentration was made such that $l^* = 500$ microns. The length of the sample holder was changed to obtain required optical thicknesses. Light was incident on one face (the front face) and the light that traversed the medium and emerged from the back face was collected by a lens and focussed onto an iris that was opened to a small extent so that predominantly the forward scattered photons were let through. This spatial filtering was carried out in order to select the forward scattered photons only which are responsible for image-formation in fourier spatial filtering techniques and temporal imaging techniques. The spatially filtered light was passed through a fixed analyser and collected by a CCD. The CCD used was an 8 bit, 256 grayscale level CCD with external control of the gain.

5.3 Data analysis

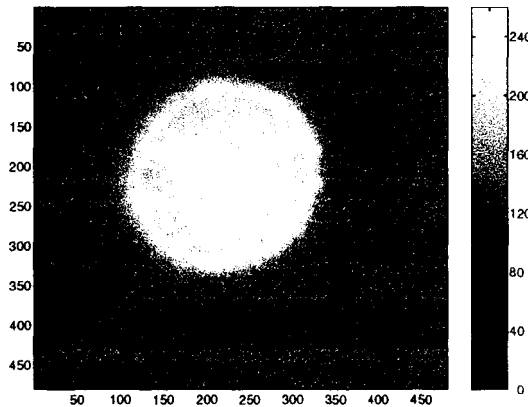


Figure 5.2: *The transmitted spot of the laser beam through the turbid medium. Shown alongside is the grayscale colorbar which is an indicator of the intensity values stored by the various pixels. Only the central area in the spot is chosen for analysis.*

The Figure 5.2 shows the transmitted beam as seen by the CCD camera, in absence of a scattering medium. A rectangular area of 150 by 150 pixels within the central spot was

chosen, and the intensity of recorded light was averaged over the pixels within the area to get the mean intensity at a polariser position. This was done for various orientations of the polariser. Thus, after grabbing a series of frames for time T , we built a time series of intensity values of the light transmitted through the medium. The above time series is fourier transformed.

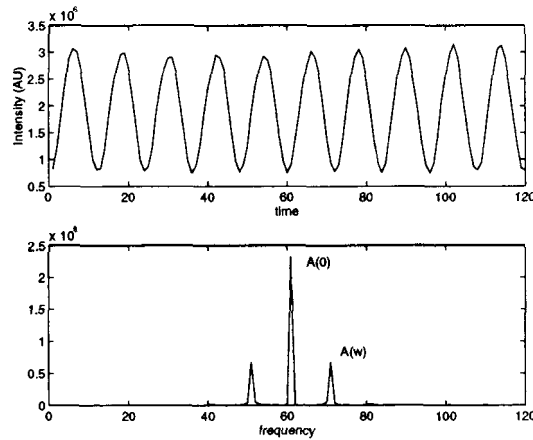


Figure 5.3: The upper subplot shows the time series of the intensity averaged over the illuminated pixels as a function of time, i.e., a function of the analyser position. The fourier transform of this time series leads to the profile shown in the lower subplot. The amplitude at zero frequency, $A(0)$, corresponds to the total intensity while the other peak, at the frequency 2ω corresponds to the polarised intensity.

Figure 5.3 shows a part of a typical timeseries and the fourier transform of that part. As expected, the FFT shows three peaks, characteristic of the fourier transform of a cosine-squared function. There is one peak at the zero frequency having amplitude A_0 , and two other peaks, symmetrically placed at the frequencies 2ω and -2ω , having amplitude A , each. The zero frequency component corresponds to the total intensity of transmitted light falling on the detector integrated over the time T . The amplitude A corresponds to the light intensity that varies cosinusoidally with the frequency 2ω , effectively, the amount of light that preserved its polarisation. Thus, these quotients A_0 and A , quantified the total transmitted intensity and the intensity of the polarisation preserving light, respectively. In the absence of any scattering medium, the transmitted light is entirely ballistic. In this case, the amplitude of each of the two peaks at A , is equal to $\frac{1}{2}A_0$. Upon addition of

scatterers, the ratio $\frac{A_\omega}{A_0}$ goes below $\frac{1}{2}$ since some of the ballistic light is depolarised, and is treated as noise, reducing A , and increasing A_0 . The amplitudes A_0 and A_ω were obtained by carrying out the above procedure for various optical thicknesses τ , for suspensions of different scattering anisotropies.

This procedure is fundamentally similar to the one mentioned in the chapter 3, where we described our scheme of imaging through turbid media. Here, instead of a shadow, we allow a flat intensity beam to transmit through the scattering medium and illuminate a certain part of the CCD. To save experimental and computational time and to minimise any spurious count that may arise due to the speckle from surrounding equipment, we avoid pixel-by-pixel analysis of the intensity distribution on the CCD, but rather, average the entire intensity falling onto the area of interest. This yields a single scalar, that is used as an indicator of the transmitted intensity.

5.4 Experimental results

We now discuss the results obtained from the experiments, and examine their implications on the process of imaging through turbid media.

The figure 5.4 shows the variation of $A_\omega(\tau)$ (solid curve), the polarised intensity, and $A_0(\tau)$ (dashed curve), the total forward scattered intensity, with optical depth τ for a sample of $g = 0.45$. The decay of $A_\omega(\tau)$ is exponential, and occurs at the length scale of the scattering mean free path, as given by the slope of the straight line. This shows the predominance of ballistic light in $A_\omega(\tau)$, which is known to decay exponentially as $\exp(-\frac{\tau}{l_s})$. The decrease in the total transmitted intensity through the forward scattering cone is slower than that of $A_\omega(\tau)$, as seen from the figure. This light contains, in addition to the polarisation preserving ballistic photons, forward scattered depolarised photons, and also the photons that undergo multiple scattering but exit the sample within the forward scattered cone. Similar trends were shown by suspensions of more anisotropic scatterers also. Imaging done by fourier filtering methods extract out the forward scattered light

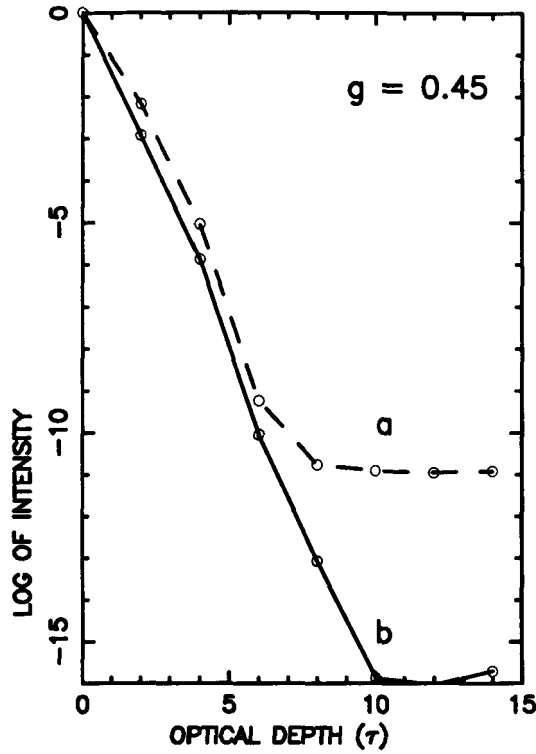


Figure 5.4: Curve a shows the experimentally observed variation of the total transmitted intensity for the particle size 0.23μ , while the curve b shows the polarised intensity.

within an angular window decided by the pinhole. The profile of $A_0(\tau)$ indicates the amount of signal collected by the fourier filtering apparatus in our experiment. Time-gating methods also select the same signal[20], except for the photons that exit within the forward scattered cone after travelling a tortuous path inside. The curve $A_0(\tau)$ can be seen to flatten out at an optical thickness of ~ 6 , beyond which the total forward scattered intensity decreases very slowly as a function of τ . On the contrary, the profile of $A_\omega(\tau)$ continues to decrease rapidly upto the thickness of $\tau \sim 10$.

It is apparent from the figure 5.4 that, out of the total forward scattered light, the technique of polarisation gating discards the frequently scattered photons which get depolarised. The profile of $A_\omega(\tau)$ becomes horizontal at around $\tau = 10$ because the CCD is no longer capable of resolving the small amplitude oscillations of the polarisation preserving signal that rides on a high noise level. It may be remarked here, that, with a CCD of

better resolution, we expect the curve to flatten out at larger optical thicknesses. The implications of these results on imaging are as follows. The effect of the forward scattered light on the image is that, due to the off-axis travel of these photons within the medium, the resolution and the contrast of the image is reduced. The ideal image is formed by the ballistic light, which is extracted better by polarisation gating, as shown by the figure 5.4. Till about $\tau = 6$, the fourier gate behaves similar to the polarisation gate, as is obvious from the fact that the profile of $A_0(\tau)$ follows the ballistic decay upto $\tau = 6$ in figure 5.4. After $\tau = 6$, $A_0(\tau)$ is dominated by the forward scattered photons or the snake photons, and the "noise" photons, which have undergone scattering, and emerged on axis, and hence have passed through the spatial filter. Indeed, in temporal imaging, the snake photons are considered useful because of their near-forward propagation. Accordingly, temporal imaging yields images with blurred edges, and low contrast. Polarisation gating, however, discards the snake photons due to their depolarisation, and results in better images, that have better resolution and contrast. Thus, from figure 5.4, images obtained by fourier (temporal) gating at $\tau = 6$ or larger optical depths will be noisy due to the snake photons. The images obtained at the same optical depths by polarisation gating will be cleaner. Thus, polarisation gating can be used to clean the images obtained by other methods.

The comparative results for different scattering anisotropies is shown in figure 5.5. From the curves plotted for $g = 0.117, 0.302, 0.375$ and 0.45 , it can be clearly seen that polarisation is preserved upto larger optical depths in media composed of isotropic scatterers. Similar behaviour was recently reported in an experimental study of the degree of polarisation inside scattering phantoms and biological tissues[21]. The results in that article for the depolarisation of linearly polarised light in aqueous suspensions of polystyrene microspheres agrees with our experimental findings in the case of the above three scattering anisotropies. This is evidently due to the fact that the process of polarisation discrimination picks out the ballistic light which, in an anisotropic scattering medium, decays faster due to the shorter mean free path. This is because, for a given l^* , the l_s for an anisotropic medium is smaller than the l_s for an isotropic medium. Consequently, it is

easier to image deeper inside the isotropically scattering sample using the polarisation memory of ballistic photons.

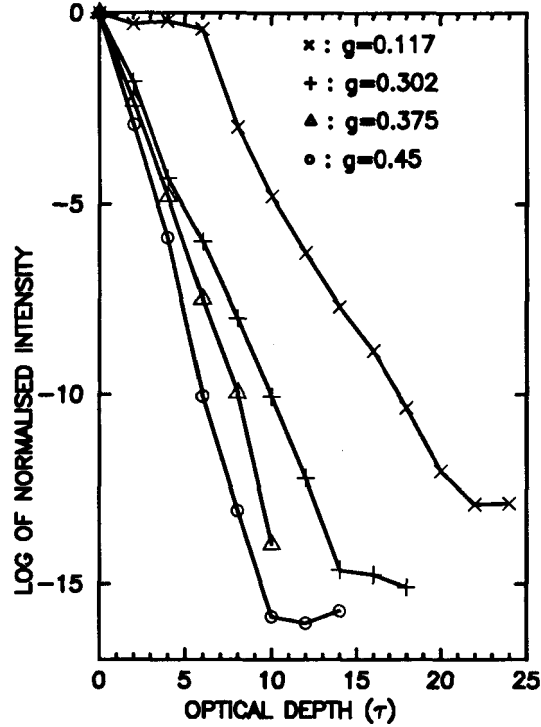


Figure 5.5: Experimentally observed variation of the polarised intensity as a function of the optical depth $\tau = \frac{l}{l^*}$ for four different particle sizes, $x : 0.12\mu$, $+ : 0.192\mu$, $\Delta : 0.21\mu$ and $o : 0.23\mu$. The respective anisotropy parameters are given in the figure.

The figure 5.6 shows the decay of $A_\omega(\tau)$ and $A_0(\tau)$ for three different anisotropies. Two observations are of interest here. In the first case, where $g = 0.117$, we can image to a depth of about $20l^*$ inside the sample using the current experimental setup, as compared to a depth of only about $10l^*$ for a sample of $g = 0.45$, since even at these depths, the polarised ballistic light is too weak to be detected. The second observation is regarding the optical depth at which the curves for $A_\omega(\tau)$ and $A_0(\tau)$ flatten out. For the sample of $g = 0.117$, the profile of $A_0(\tau)$ starts deviating from the ballistic decay at around $\tau = 12$. $A_\omega(\tau)$ stabilises at around $\tau = 20$, due to the limited CCD resolution. For the sample with $g = 0.45$, the same happens at $\tau = 6$ and $\tau = 10$ respectively. As $A_0(\tau)$ represents the signal observed in temporal gating, and $A_\omega(\tau)$ that with polarisation discrimination, for

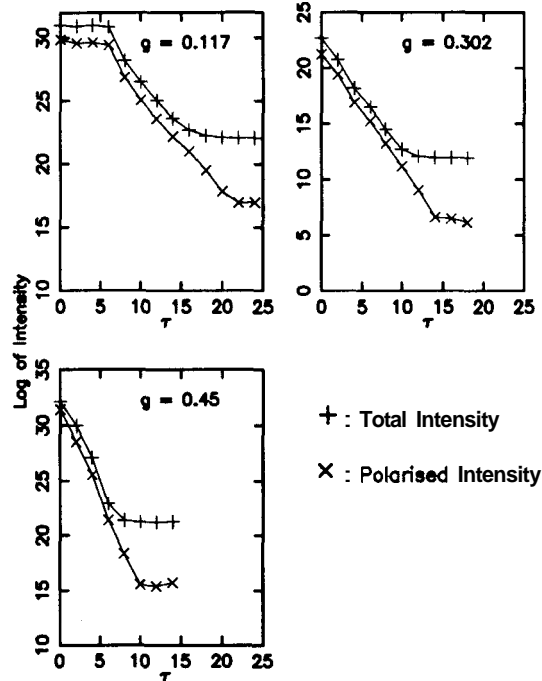


Figure 5.6: The difference between the decay of the polarised intensity and the decay of the total forward scattered intensity observed experimentally, for three different particle sizes; 0.12μ , 0.192μ and 0.23μ .

a given experimental setup, the process of polarisation gating cleans the images obtained by temporal gating over a larger range of optical thickness in samples of more isotropic scatterers.

These experimental findings give us an estimate of the depth of imaging using polarisation gating, and also about the efficiency of the process for samples of different anisotropies. However, the experiments suffer from a few drawbacks like the limited sensitivity, resolution and the dynamic range of the CCD, the unwanted speckle arising from the surrounding apparatus, and the stray light. In our experiments, the **CCD** limitations are particularly important. As can be realised from the experimental procedure, in our experiments, the intensity falling on the **CCD** varies from a minimum to a maximum through a cosine-squared function. This is true for data gathered for each optical thickness and each scattering anisotropy. To ensure that the intensity variation falling on the **CCD** is within its dynamic range (so as to avoid spurious readings) for each optical thickness

and anisotropy, it is essential to employ certain combinations of attenuators along with variation of the CCD gain. It is also important to carefully choose various normalisation constants in the course of data analysis.

Due to these limitations, we proceeded to investigate the problem numerically, through a series of Monte Carlo simulations. We could study the process of polarisation preservation for a larger range of optical thicknesses, and scattering anisotropies. We now describe the numerical experiment, its results, and discuss their implications.

5.5 Numerical simulations

After obtaining the above results experimentally, to gain a physical understanding of the differing rates of depolarisation and their non-monotonic dependence upon anisotropy, we proceeded to investigate the problem numerically, through a series of extensive Monte Carlo simulations. This facilitated the study of light transport over a larger range of optical thicknesses. Monte Carlo simulations have been used earlier to study transport of polarised light through scattering media, especially in the context of imaging through turbid media[20]. The essence of the method involves simulating the particle trajectories as it performs a three-dimensional random walk inside the scattering medium. The scattering angle distributions, path-length distributions and other parameters are generated depending upon the characteristics of the scattering medium. Though computationally very expensive, this technique is robust, easy to implement and provides a free handle on various physical parameters involved in the process being simulated.

We recall the first principles of representing and studying polarised light using Stokes parameters and Mueller matrices. The chapter 2 discusses the fundamentals of Stokes parameters and Mueller matrices, and also enlists the techniques of determining them. More detailed treatments are available in reference [22]. For a beam of linearly polarised light, whose polarisation vector is defined in the XY plane of a certain general XYZ frame of reference, if E_x and E_y are the two orthogonal components of the electric field, the

polarisation state of the light is represented by the Stokes vector

$$\mathbf{I}_i = \begin{bmatrix} I \\ Q \\ U \\ V \end{bmatrix}, \text{ where the Stokes parameters } I, Q, U \text{ and } V \text{ are given by}$$

$$I = E_x E_x^* + E_y E_y^* \quad (5.1)$$

$$Q = E_x E_x^* - E_y E_y^* \quad (5.2)$$

$$U = E_x E_y^* + E_y E_x^* \quad (5.3)$$

$$V = i(E_x E_y^* - E_y E_x^*) \quad (5.4)$$

The polarisation of such a beam changes upon scattering, and the relation between the input and the output Stokes vectors is given by

$$\mathbf{I}_o = \mathbf{M}(\theta, \phi) \mathbf{I}_i, \quad (5.5)$$

where $\mathbf{M}(\theta, \phi)$ is the Mueller matrix given by equation 2.26, θ is the scattering angle and ϕ is the azimuth of the scattering plane.

A transformation is due, to transform the Stokes vector which is defined relative to a certain plane before scattering, to a vector defined relative to the scattering plane. The transformation is done by the matrix $\mathbf{R}(\phi)$ given by

$$\mathbf{R}(\phi) = \begin{bmatrix} 1 & 0 & 0 & 0 \\ 0 & \cos 2\phi & \sin 2\phi & 0 \\ 0 & -\sin 2\phi & \cos 2\phi & 0 \\ 0 & 0 & 0 & 1 \end{bmatrix} \quad (5.6)$$

When an input beam with the Stokes vector \mathbf{I}_i interacts with an ideal linear polariser, whose transmission axis makes an angle ξ to the direction along the parallel component of the electric field, the Stokes vector of the output beam \mathbf{I}_o is given by the transformation

$$\mathbf{I}_o = \mathbf{M}(\xi) \mathbf{I}_i \quad (5.7)$$

where $\mathbf{M}(\xi)$ is the Mueller matrix of the polariser, given by equation 2.24.

We followed the conventional algorithm of Monte Carlo simulations used earlier for scalar wave transport, but kept track of the Stokes vector of the photon and its evolution through Mueller matrices. The system we modelled was that of a suspension of microspheres. The positions of the microspheres were randomly distributed, yet there was no initial random configuration that was frozen so as to make the photons scatter off a given set of random positions. Every new scattering centre was picked out independently from a random distribution. No effects of the motion of scatterers was included. The geometry used for the simulation is shown in the figure 5.7.

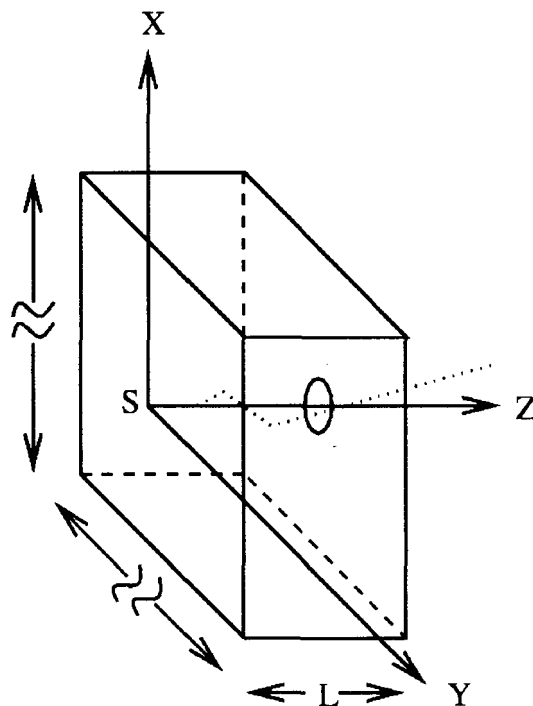


Figure 5.7: The geometry used in the simulations. S is the source of photons placed at $(0, 0, 0)$ of a semi-infinite slab of a scattering medium. The beam is directed along $+Z$ axis. The dotted line shows a probable photon path.

A slab of a scattering medium was considered, whose extent was infinite along the $+X$ and the $+Y$ axis. A beam of zero width was simulated by launching photons from a single point on the input face of the semi-infinite slab, thereby simulating an ideal point source. The position \mathbf{r}_0 , given by $\mathbf{r}_0 = (0, 0, 0)$, was taken as the point of launch for each photon. Each photon underwent elastic scattering at various random sites \mathbf{r}_i inside the random

medium. An elastic scattering event merely implied a sudden change in direction without absorption. This change was also calculated through relevant probability distribution.

Between any two scattering events, the photon traversed a straight line path with length l_i . The pathlength distribution of photons inside a random sample of scattering mean free path l_s was given by

$$P(l_i) = \frac{1}{l_s} \exp\left(-\frac{l_i}{l_s}\right). \quad (5.8)$$

This pathlength distribution was simulated by $l_i = -l_s \ln \text{RAN}$, where RAN was a random number uniformly distributed over the interval $(0, 1)$. At each scattering site \mathbf{r}_i , the photon changed its initial direction and was propelled into a new direction (θ_i, ϕ_i) . The direction of travel was picked up from the relevant distributions, as described below.

At the zeroth site, i.e., at the position of launch of the photon, the direction of travel was taken to be $(\theta_0, \phi_0) = (0, 0)$, which simulated a ballistic beam parallel to $+Z$ axis. As mentioned earlier, the angle of scattering depends upon the size of the particles, and forward scattering is preferred as the particle size becomes larger than the wavelength. This anisotropy in scattering is reasonably represented by the Henyey-Greenstein (H-G) distribution[23] for the angle of scattering θ , given by

$$P(\theta) = \frac{1 - g^2}{(1 + g^2 - 2g \cos \theta)^{3/2}} \quad (5.9)$$

Here, g is the anisotropy parameter as explained earlier. The H-G phase functions are simple to compute as compared to the exact Mie phase functions. The illustration 5.8 compares the behaviour of the Mie phase function and the H-G phase function, for three different particle anisotropies. The deviations from the Mie phase functions can be traded off with the computational simplicity of the H-G phase functions.

Corresponding to the scattering anisotropy of the microparticles, a Henyey-Greenstein distribution was constructed, from which the scattering angles θ_i were picked up.

Here, we would like to stress the fact that the dependence of the angle of scattering

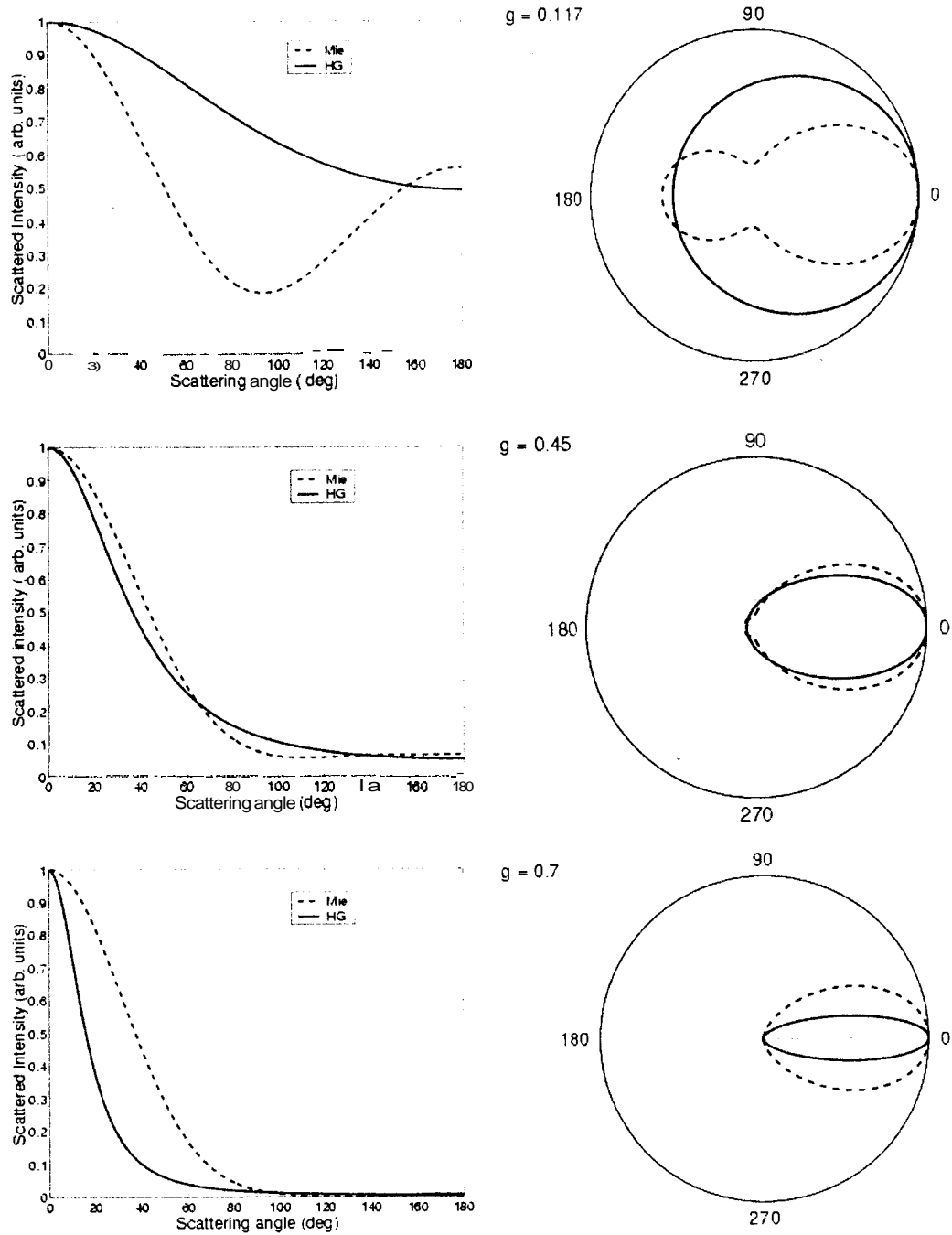


Figure 5.8: Comparison of the Henyey-Greenstein and Mie phase functions for three different anisotropies.

on the initial polarisation state of the photon had been omitted due to the use of the Henyey-Greenstein approximation. The exact Mie theory gives a clear difference between the distribution of angle of scattering when the initial polarisation state of the photon is parallel and that when it is perpendicular, where parallel and perpendicular are defined with respect to the scattering plane. However, the theory can provide the scattering angle distribution only in these two cases, and generating a distribution for an arbitrary polarisation state requires keeping track of the two orthogonal components, as well as the phase difference between them. So, we choose to use the approximation given by Henyey and Greenstein, as has been done in earlier published work.

The choice of ϕ_i was done from a uniform distribution over 4π steradian. Ideally, one needs to weigh the chosen ϕ_i by the actual power scattered per unit solid angle in the direction with that value of ϕ_i . However, choosing an equiprobable ϕ_i has been shown to give negligible errors when the number of scattering events was larger than a few units[24]. Furthermore, as shall be clear from the following description, our Monte Carlo simulation involved launching of photons with linear polarisation at various angles from the horizontal. Thus, a kind of ergodicity was introduced in the sense that, certain azimuthal angles that were improbable for a given state of linear polarisation, were completely allowed for another state. This reduced the errors that were generated in the case of transport involving lesser scattering events.

The angles of scattering were always chosen with respect to the initial direction of propagation of the photon, i.e., defined on a local coordinate frame whose origin was at the position of the photon. We needed to record the coordinates of the photon with respect to the global frame, where the $+Z$ axis was the direction of the launch of the beam, and the sample was infinite along the X and Y axes. After each scattering event, the scattering angle θ was calculated in the local coordinate frame which was chosen to be a spherical coordinate system for ease of calculations. For a chosen pathlength l and the scattering angle θ and the azimuth ϕ , the local coordinates $[x_{loc}, y_{loc}, z_{loc}]$ are given by

$$x_{loc} = l \sin \theta \cos \phi \quad (5.10)$$

vector \mathbf{S}_i , which was then transformed back to the general XYZ frame using $\mathbf{R}(-\phi_i)$, since that was the plane with respect to which the polarisation states were defined.

At a single orientation of the polariser, a set of 10^7 photon paths was simulated, along with the evolution of polarisation. The intensity of the photons crossing the output polariser was collected for various states of input polarisation by varying orientation of the input polariser in steps of 10° . Similar to the experimental procedure, a series of varying intensity values was obtained and fourier transformed to extract the amplitudes A , and A_0 , which were proportional to the polarisation preserving intensity and the total intensity falling onto the detector, respectively. These amplitudes were obtained for various optical thicknesses, and for different scattering anisotropies. The results that we obtained from the simulations elucidate the difference between the depolarisation rates of the ballistic light and the forward scattered light.

5.6 Simulation results

Upon investigating a larger range of sample thickness and particle sizes in our Monte-Carlo simulations, we obtained results which agreed with the experimental inferences, and further elucidated the effect of the polarisation gate. Figure 5.9, which shows simulation results for $g = 0.302$, shows the variation of the total intensity and the polarised intensity as a function of optical depth. The curve *a*, representing the polarised intensity, decays initially upto $\tau = 7$. Then we notice a change in the rate of decay at $\tau = 7$. After that, the decay is slower. The ballistic decay is shown in the figure by a dash-dotted line. Upon comparison with the curve *a*, we see that the polarised light intensity, indeed, consists of the ballistic light, and decays almost at the rate of ballistic decay. The slight and steady deviation is a result of weakly scattered photons which still preserve their polarisation. This deviation is expected to reduce in more isotropic suspensions and increase in more anisotropic suspensions. The curve *b* shows the reduction in the total forward scattered intensity. This light would be the signal for a fourier gate or a temporal gate. This signal

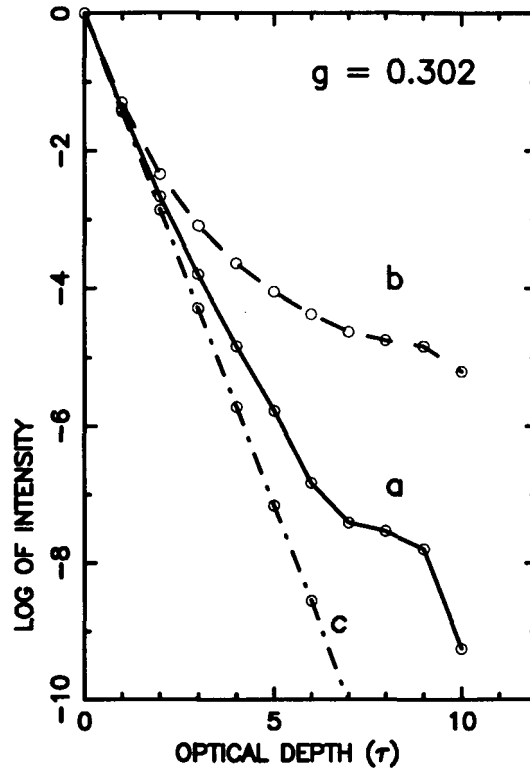


Figure 5.9: The variation of the polarised intensity(a) and the total intensity(b) for a particle size of 0.192μ , as seen from the numerical simulations. The dash-dotted straight line corresponds to the decay of ballistic light in such a sample.

also carries the ballistic light, but, it is overwhelmed by the photons scattered in the forward direction, as is obvious by the deviation of curve b from the ballistic line. These photons hit the detector off-axis, and smear out the image yielded by the ballistic light thus damaging the contrast and its resolution.

The dependence of this variation on anisotropy is clarified from the plots in figure 5.10: where the simulation results for A_{ω} and A_0 are plotted for four different anisotropies. The ballistic decay in each case is also shown by the solid straight line in the subplots. As can be seen, the deviation of A_{ω} from the ballistic decay is smaller in the case of isotropic scatterers, and larger in the case of anisotropic scatterers. Furthermore, the deviation of A_{ω} from A_0 is least in the isotropic scatterers. The process of polarisation gating can separate out the ballistic photons from the total forward scattered signal in these

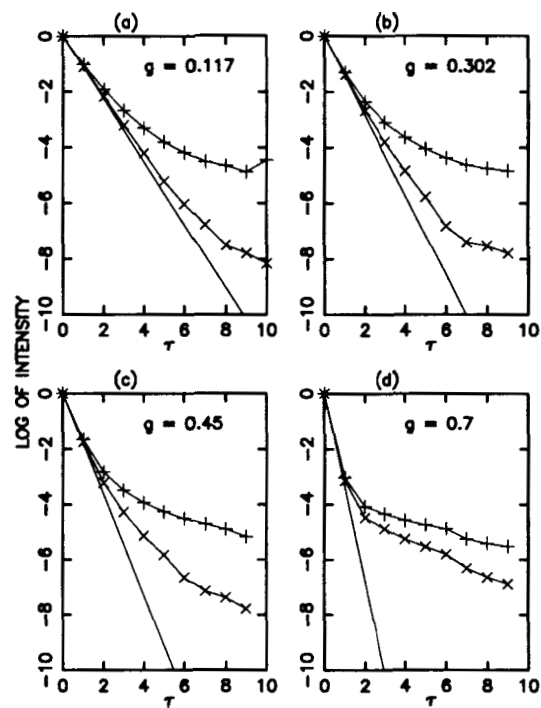


Figure 5.10: Comparison of the polarised intensity and the total forward scattered intensity, as seen from the simulations, for four different particle sizes, (a) : 0.12μ , (b) : 0.192μ , (c) : 0.23μ and (d) : 0.3μ . x : polarised intensity; $+$: total forward scattered intensity. The solid line shows the ballistic decay in each case.

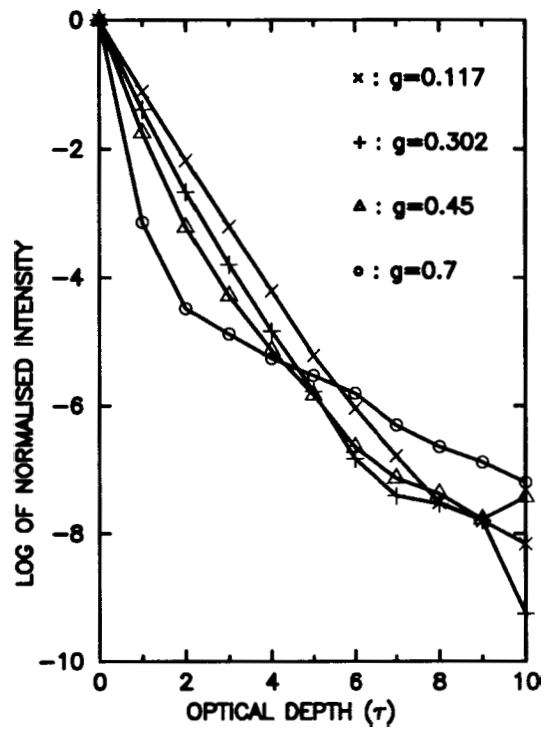


Figure 5.11: The behaviour of the polarised intensity for four different particle sizes, as observed from the simulations. x : 0.12μ , $+$: 0.192μ , Δ : 0.23μ and o : 0.3μ .

scatterers. As the scatterer size increases, the two curves, A_+ and A_0 , tend to behave similarly, as is the case in Fig 5.10(d). This is due to the fact that the ballistic light gets converted to forward scattered light at a very small optical thickness inside the medium with large scatterers. So, the light that is extracted by polarisation discrimination also consists largely of the forward scattered photons. As a result, the fourier-filtered signal is not too different from the polarisation-filtered signal. This is in agreement with our experimental inference, where we mentioned that in case of anisotropic scatterers, the range of optical depths over which images can be cleaned using polarisation gating is smaller, as compared to isotropic scatterers.

Figure 5.11 shows the comparative trends in the decrease of the polarised intensity between $g = 0.117, 0.302, 0.45$ and 0.7 . In each of the above cases, one can see a rapid decay in the polarised light intensity upto a certain optical thickness, after which the decay rate reduces, understandably due to the predominance of forward scattered photons over the ballistic photons. Note that the curve corresponding to $g = 0.7$ actually crosses the other curves as its decay rate becomes small.

The difference in the behaviour of the temporal/fourier gate and the polarisation gate is made clearer by the figures 5.12 and 5.13, where the light intensity is plotted as a function of $\frac{L}{l_s}$. For all the four anisotropies, there is no significant difference in the total forward scattered intensity which is shown by figure 5.12. This is the signal for the temporal or the fourier gate. The fourier and the temporal gates do not distinguish between scatterers of different anisotropies. The figure 5.13 shows the variation of the polarised light intensity as a function of $\frac{L}{l_s}$. Initially, one can see that the polarised intensity decays at the same rate for all samples, which is, again, understandable because of the predominance of the ballistic light in the signal. Later, at $\frac{L}{l_s} \sim 7$ in the figure 5.13, the signal from the anisotropic sample is adulterated by the forward scattered light. Larger the anisotropy, more is the content of the forward scattered light in the signal. This forward scattered light degrades the image resolution and contrast by reaching the regions of the geometric shadow of the object. The signal from isotropic sample, however, consists of the ballistic

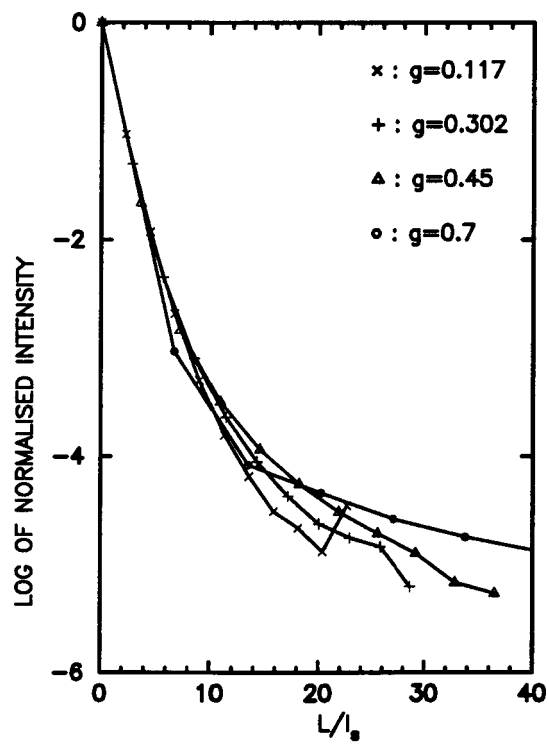


Figure 5.12: Simulation results for the variation of the total forward scattered intensity as a function of $\frac{L}{l_s}$ for four different particle sizes, x : 0.12μ , $+$: 0.192μ , Δ : 0.23μ and o : 0.3μ .

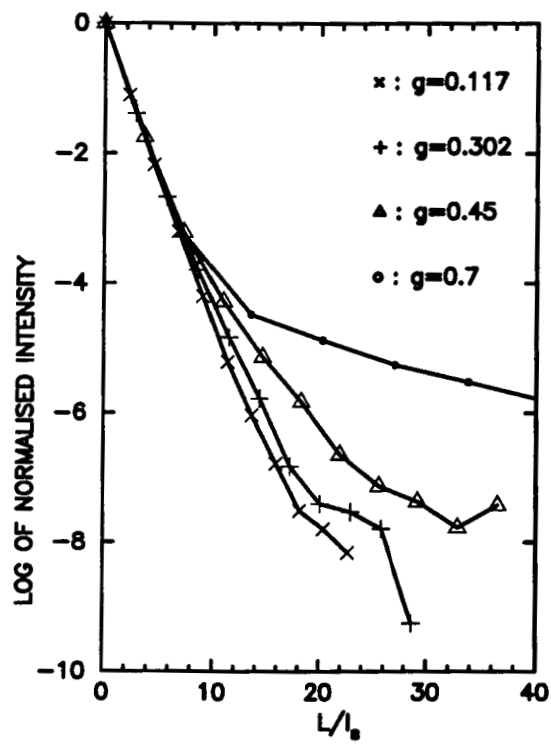


Figure 5.13: Simulation results for the variation of the polarised intensity as a function of $\frac{L}{l_s}$ for four different particle sizes, x : 0.128 , $+$: 0.192μ , A : 0.23μ and o : 0.3μ .

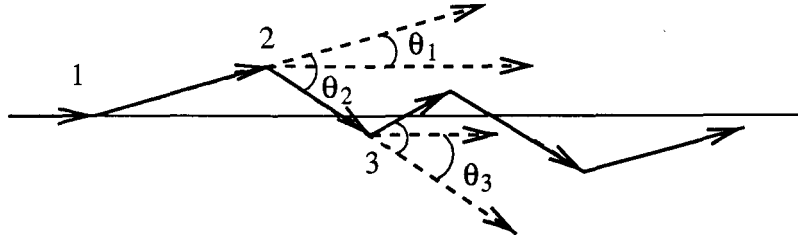


Figure 5.14: *Depolarisation of the snake photons. The bold line shows a possible trajectory of a snake photon. After scattering from site 1, the photon travels at an angle θ_1 with respect to the incident direction. It gets scattered through an angle θ_2 from the site 2, but with respect to the incident direction, the change in direction of propagation is only through an angle θ_3 . The change in polarisation, however, is proportional to the angle θ_2 . After several small angle scatterings, the forward scattered photon maintains its direction of propagation, and has a short time of flight, but is vastly depolarised.*

light only, upto larger values of $\frac{L}{l_s}$. Thus, images extracted from isotropic samples will have larger contrast, as well as better resolution. Further, the polarisation gate results in contrast enhancement and resolution enhancement of the image obtained by fourier spatial gating as well as temporal gating. As explained above, contrast enhancement and resolution enhancement is more efficient in the case of isotropic scatterers.

The physical justification of the above numerical results is as follows. It is known that scattering off an isotropic scatterer changes the polarisation of the incident light to a large extent, because the average scattering angle is large. Thus, the polarisation gate easily discards the forward scattered photons from isotropic scatterers. In case of anisotropic scatterers, the angle of scattering is small, and hence the depolarisation is small. As a results, the forward scattered photons also pass through the polarisation gate, and contaminate the ballistic signal. It is of importance to note that forward scattering affects the direction of propagation and the polarisation differently. Note figure 5.14 for the illustration of this fact. The change in polarisation is proportional to the change in the direction of propagation, with respect to the direction of propagation prior to the scattering event. The mean direction of propagation, however, remains more or less parallel to the initial direction of ballistic light. Thus, photons that undergo a few small angle scattering events still persist in the near-forward direction and hence have short pathlengths, but are

greatly depolarised. This is the underlying cause of the larger efficiency of the polarisation gate over fourier and temporal gates.

Thus, we complement our earlier result which proved that it is easier to image deeper inside a sample comprising of isotropic scatterers. Polarisation discrimination can be used to extract the ballistic content inside the forward scattered light to achieve better resolution and higher image contrast. The polarisation filter is efficient in the case of isotropic scatterers where very few scattering events depolarise the photon to a large extent. In the case of anisotropic scatterers, the forward scattered light is depolarised to a small extent only, and hence is not filtered by the polarisation gate.

This study helps in gauging the depth of imaging inside media of varying anisotropies, and also in making a choice as to the right source brightness, detector resolution etc. Further, it sheds light on the depolarisation of polarised light in the random medium, in a regime where analytical theory is short of definitive conclusions. We believe that polarisation and depolarisation upon multiple scattering can provide a handy tool for studying the most elusive regime of scattering, that with a few scattering events, but still short of the diffusion regime.

5.7 Conclusions

We have experimentally studied the transport of polarised light through slabs of random media of varying optical depths, and different scattering anisotropies. We devised a scheme of quantifying the polarised fraction of transmitted light and used this method to study the depolarisation of photons as a function of scattering thickness. We have shown through our numerical studies that the polarisation gate is capable of extracting the ballistic light from the quasiballistic light. We have applied our results to imaging through turbid media, and shown that polarisation can be used to improve the resolution and the contrast of the image obtained from the quasiballistic light, by either fourier gating, or temporal gating. The polarisation gate has been shown to perform well in case of isotropic scatterers, and is

has a limited use in case of anisotropic scatterers. We believe that this method of tagging the photons by their polarisation provides a means to study the snake photons inside the scattering medium.

Bibliography

- [1] *Scattering and localisation of classical waves in random media*, ed. Ping Sheng, (World Scientific, Singapore 1990).
- [2] A. Ishimaru, *Wave propagation and scattering in random media Vol I & II* (Academic, New York, 1978).
- [3] S. Chandrasekhar, *Radiative transfer* (Clarendon Press, Oxford, 1961).
- [4] E. Akkermans, P. E. Wolf and R. Maynard, Phys. Rev. Lett. 56, 1471 (1986).
- [5] M. J. Stephen and G. Cwilich, Phys. Rev. B 34, 7564 (1986).
- [6] M. B. van der Mark, M. P. van Albada, and Ad Lagendijk, Phys. Rev. B 37, 3575 (1988).
- [7] S. Feng, C. Kane, P. A. Lee and A. D. Stone, Phys. Rev. Lett. 61, 834 (1988).
- [8] J. H. Page, H. P. Schreimer, A. E. Bailey and D. A. Weitz, Phys. Rev. E 52, 3106 (1995).
- [9] Isaac Freund, Moshe Kaveh and Michael Rosenbluh, Phys. Rev. Lett. 60, 1130 (1988).
- [10] D. A. Weitz, D. J. Pine, P. N. Pusey and R. J. A. Tough, Phys. Rev. Lett. 63, 1747 (1989).
- [11] K. M. Yoo and R. R. Alfano, Opt. Lett. 15, 320 (1990).
- [12] K. M. Yoo, Feng Liu and R. R. Alfano, Phys. Rev. Lett. 64, 2647 (1990).

-
- [13] D. J. Durian and J. Rudnick, *J. Opt. Soc. Am.* 14, **235 (1997)**.
- [14] A. A. Chabanov and A. Z. Genack, *Phys. Rev. E* 56, **R1338 (1997)**.
- [15] K. K. Bizheva, A. M. Siegel and D. A. Boas, *Phys. Rev. E* 58, **7664 (1998)**.
- [16] Z. Q. Zhang, I. P. Jones, H. P. Schreimer, J. H. Page, D. A. Weitz, and Ping Sheng ,
Phys. Rev. E 60, **4843 (1999)**.
- [17] Thorsten Spott and Lars O. Svaasand, *Appl. Opt.* 39, **6453 (2000)**
- [18] H. Ramachandran and A. Narayanan, *Opt. Commun.* 154, **255 (1998)**.
- [19] Venkatesh Gopal, Sushil Mujumdar, Hema Ramachandran and Ajay Sood, *Opt. Commun.* 170, **331 (1999)**.
- [20] Q. Z. Wang, X. Liang, L. Wang, P. P. Ho and R. R. Alfano, *Opt. Lett.* 20, **1498 (1995)**.
- [21] Vanitha Sankaran, Klaus Schonenberger, Joseph T. Walsh Jr and Duncan J. Maitland,
Appl. Opt. 38, **4252 (1999)**.
- [22] Absorption and scattering of light by small particles, C. F. Bohren and D. R. Huffman
(Wiley, New York, **1983**).
- [23] L. C. Henyey and J. L. Greenstein, *Astrophys.J.* 93, **70 (1941)**.
- [24] P. Brusaglioni, G. Zaccanti and Q. Wei, *App. Opt.* 32, **6142 (1993)**.